Spectral Angle Mapper and aeromagnetic data integration for gold-associated alteration zone mapping: a case study for the Central Eastern Desert Egypt

Article *in* International Journal of Remote Sensing · April 2016

DOI: 10.1080/01431161.2016.1165887

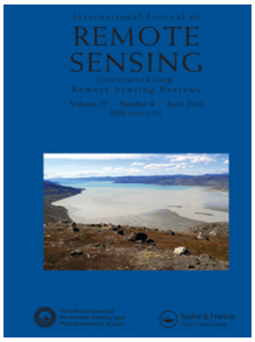

International Journal of Remote Sensing

ISSN: 0143-1161 (Print) 1366-5901 (Online) Journal homepage: http://www.tandfonline.com/loi/tres20

Spectral Angle Mapper and aeromagnetic data integration for gold-associated alteration zone mapping: a case study for the Central Eastern Desert Egypt

Emad Hasan, Todd Fagin, Zeinhom El Alfy & Yang Hong

INTERNATIONAL JOURNAL OF REMOTE SENSING, 2016
VOL. 37, NO. 8, 1762–1776
http://dx.doi.org/10.1080/01431161.2016.1165887

Spectral Angle Mapper and aeromagnetic data integration for gold-associated alteration zone mapping: a case study for the Central Eastern Desert Egypt

Emad Hasan [a,d], Todd Fagin[b], Zeinhom El Alfy[c] and Yang Hong[a]

[a]Hydrometrology and Remote Sensing (HyDROS) Laboratory, Advanced Radar Research Center (ARRC), University of Oklahoma, Norman, OK, USA; [b]Department of Geography and Environmental Sustainability, University of Oklahoma, Norman, OK, USA; [c]Egyptian Geological Survey and Mining Authority, Cairo, Egypt; [d]Geology Department, Faculty of Science, Damietta University, New Damietta, Egypt

ABSTRACT

The Spectral Angle Mapper (SAM) classification technique is integrated with the surface structure and aeromagnetic data to map the potential gold mineralization sites associated within alteration zones in Central Eastern Desert (CED), Egypt. The surface reflectances of the Enhanced Thematic Mapper Plus (ETM+) and the Advanced Spaceborne Thermal Emission and Reflection Radiometer (ASTER) data were classified using the SAM classifier. Five spectral reflectance curves of the alteration minerals (haematite, illite, kaolinite, chlorite, and quartz) were utilized as end-members for the SAM classification. The surface lineation, and shear zone systems were delineated using ETM+ bands. The deep-seated faults were defined using the Euler deconvolution filter on the gridded aeromagnetic data. The magnetic data analysis inferred the subsurface structural depths range from 500 m to 2000 m. Geographic information system (GIS) overlaying operation was performed using the surface lineation and the subsurface faults layers to identify the structural continuity and to extract the possible migratory pathways of the hydrothermal solutions. Within Multiple Criteria Decision Analysis (MCDA), fuzzy membership operations were applied to identify the prospective alteration sites. The mapped results were compared with global positioning system (GPS) locations of existing alteration zones. The current proposed mapping method is considered a robust tool for decision-making and potential site selection technique for further mineral exploration in CED.

ARTICLE HISTORY
Received 2 September 2015
Accepted 7 March 2016

1. Introduction

Gold deposits in Egypt and northern Sudan were found and exploited as early as the Predynastic times (ca. 3500 BC) (Klemm, Klemm, and Murr 2001). The ancient Egyptian miners extracted gold mineral from more than 120 sites and occurrences, each located in the Precambrian basement rock within the Central Eastern Desert (CED) and the

CONTACT Emad Hasan emad.hasan@ou.edu Hydrometrology and Remote Sensing (HyDROS) laboratory, Advanced Radar Research Center (ARRC), National Weather Center, 120 David L. Boren Blvd, suite 4646, Norman 73072, OK, USA

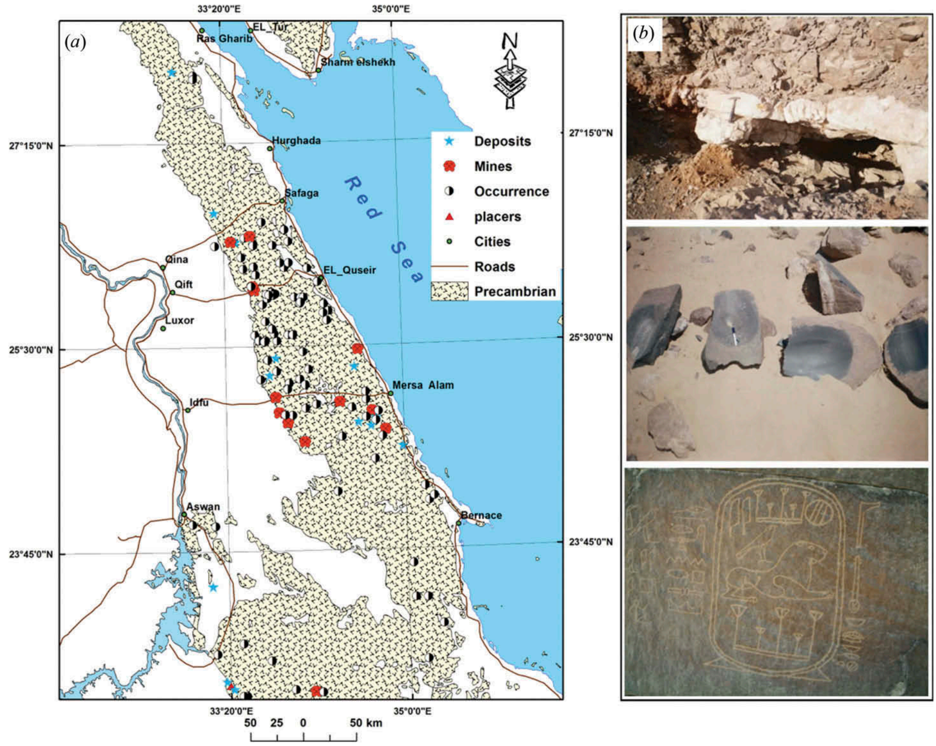

Figure 1. Gold mining activities in CED, map (*a*) shows the ancient gold sites, (*b*) field photographs show some ancient activities such as vein excavation, tools, and rock engraving.

Southern Eastern Desert (SED) (Figure 1). Most of the ancient mining activities targeted the quartz-veins gold-type deposits. Nevertheless, other reserves of gold mineral are contained and associated within the alteration zones (Botros 2004). Mapping of the potential mineralized alteration zones is a critical task to enhance mineral exploration in the CED. Previously, such mapping works had utilized standard remote-sensing techniques such as image rationing (Gabr, Ghulam, and Kusky 2010; Gad and Kusky 2006, 2007; Pour and Hashim 2012), principal component analysis (Honarmand, Ranjbar, and Shahabpour 2012; Ren and Abdelsalam 2006), and image classifications (Amer, Kusky, and El Mezayen 2012; Gabr, Ghulam, and Kusky 2010; Honarmand, Ranjbar, and Shahabpour 2012). In this study, the Spectral Angle Mapper (SAM) classification, surface structure, aeromagnetic data, and the Multiple Criteria Decision Analysis (MCDA) are used to aid for better mapping results of the prospective mineralized alterations in CED.

The SAM algorithm is a spectral classifier that calculates the similarity between two spectra by treating them as vectors in a space (Figure 2) with *n*-dimensionality equal to the number of bands (Hunter and Power 2002; Kruse et al. 1993). The angular information between pixel spectra is used as a specific threshold to classify each pixel (ENVI 2008). The pixels with angles further away than the specified maximum angular threshold in radians are not classified. This means that the closer the angle, the better the match (Kruse et al. 1993; Kruse, Richardson, and Ambrosia 1997). In SAM, reference spectra can be either taken from the available spectral libraries or field measurements or

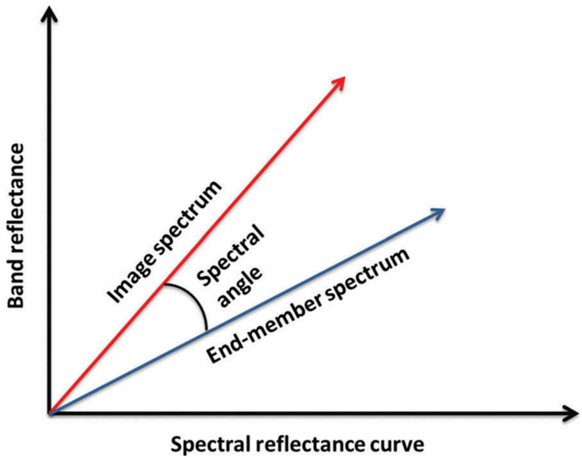

Figure 2. Illustration of the SAM supervised classification technique.

extracted as training regions of interest (ROIs) directly from the satellite imagery (Kruse et al. 1993). The SAM classifier mainly relies on the shape of the spectral pattern, and the data not required to be normally distributed. Additionally, when the SAM measures the angle between two spectral vectors it is not affected by solar illumination factors (Gupta 2003; Papp and Cudahy 2002). Generally, the SAM classification enhances the target reflectance characteristics and discriminates effectively between rocks and alteration minerals; each has its unique spectral characteristics that differentiate their signatures and help acquire more adequate mapping results.

The use of SAM with aeromagnetic data in alteration mapping has not been fully demonstrated yet. Meanwhile, the formation of alteration zones is mainly controlled by faulting and shearing systems. The hydrothermal solutions need subsurface conduits and pathways to let the fluid penetrate into the rock to chemically alter their composition and selectively deposit different precious metals. Hydrothermal activities occurred along parts of the fault zone, producing tectonically quartz veins and alteration zones, some of which contain gold, copper, zinc, silver, and lead minerals (EMRA 2006; Hussien 1990). The distribution of these veins reflects the mechanical condition associated within the faulting system (McMahon 1979). Therefore, the linear configuration features, such as surface lineation, faulting, and shearing, play an important role in localizing the alteration zones. The identification of the structural elements can be based on the surface lineation and the aeromagnetic data analysis.

The geophysical methods provide powerful tools for minerals and ores exploration (Rabeh et al. 2006; Ramadan and Sultan 2003). The aeromagnetic data are widely used; they record the variations in the intensities of the Earth's magnetic field (Telford, Geldart, and Sheriff 2001). These variations are due to the relative spatial abundance of magnetic minerals in the upper levels of crust (Telford, Geldart, and Sheriff 2001), which are linked with several mineral deposits. In practice, the elucidation of the subsurface geological structures and the shape of the rock bodies are the most valuable contributions of the aeromagnetic maps. The subsurface mapping is mainly performed through the aid of mathematical models (Hoover, Klein, and Campbell 1995). The 3D Euler deconvolution solution is an important mathematical algorithm that can be applied on gridded magnetic data to detect the faulting and geologic causal relationship (Hsu 2002). The 3D Euler deconvolution can interpret and calculate source depths depending on selected structural indices, which identify the rate of changes within the potential field at a given distance (Reid et al. 1990).

Modern geographic information system (GIS) is capable of storing, manipulating, and analysing spatial data required for the MCDA system. The Spatial Data Modeler (SDM) is a valuable GIS extension of geoprocessing tools that can perform the MCDA (Sawatzky, Raines, and Bonham-Carter 2010). The SDM includes several decision-based tools such as the weights of evidence and fuzzy logic membership operations. The fuzzy logic strategies serve as a framework to construct MCDA function sets to produce a predictive map (Kainz 2007). For instance, a fuzzy logic set f on X space measures how each criterion $\chi \in X$. The membership grade for f (χ) exists in the range of [0,1]; this grade indicates the degree to which the element χ satisfies the concept being modelled by f (Yager 2015). In each fuzzy logic set, several elements can be categorized according to their functionality, their quantification, and the weights (Kainz 2007). The fuzzy overlay is another logic method that can integrate multiple inputs to identify the target areas by computing the degree of truthfulness between each data set. Generally, the fuzzy MCDA clarifies the best selections of criteria among the input data for better decision-making.

The main objective of the current research is to investigate the application of the SAM classification, surface lineation, and the aeromagnetic data to map the potential locations for gold mineralization in CED. The gold deposits within the alteration zones in CED are not fully mapped; most of the gold storages are still unlocked and left untouched.

2. Study area and geologic setting

The study area is located in the CED between 25°15′ N and 26°00′ N, and between 33°30′ E and 34°40′ E (Figure 3). The area is accessible through a number of drainage routes and desert tracks with major asphaltic roads. The wadis are running towards two directions, with the eastward to drain at the Red Sea and the westward to drain at the Nile Valley. The area receives insufficient amount of rainfall year round with less-frequent fauna and flora. The population is extremely small, with only a few Bedouin families living in the desert.

Geologically, the CED is a very important part of the country; this is mainly attributed to the variety of rock types and the important ore deposits that it hosts. The exposed rock units display a wide range of geologic ages from Precambrian to Phanerozoic. The igneous and metamorphic rocks represent the oldest Precambrian rock units, whereas the sedimentary rocks, which are often found along the east and west flanks, are from the Phanerozoic era (Figure 4). The igneous and metamorphic Precambrian rocks consist of the nappe assemblage of ophiolite, serpentinite, meta-gabbro, and volcano-sedimentary rocks. These rocks occur as over-thrust sheets overlapping the granitic domes. All seem to be crosscutting with the calc-alkaline to alkaline per-aluminous granite plutons and some acidic plugs. The Phanerozoic sedimentary rocks are less frequent and exposed in the low-height areas along the Red Sea coast and at the down block fault areas, whereas the Nubian sandstone covers are located mainly in the western areas.

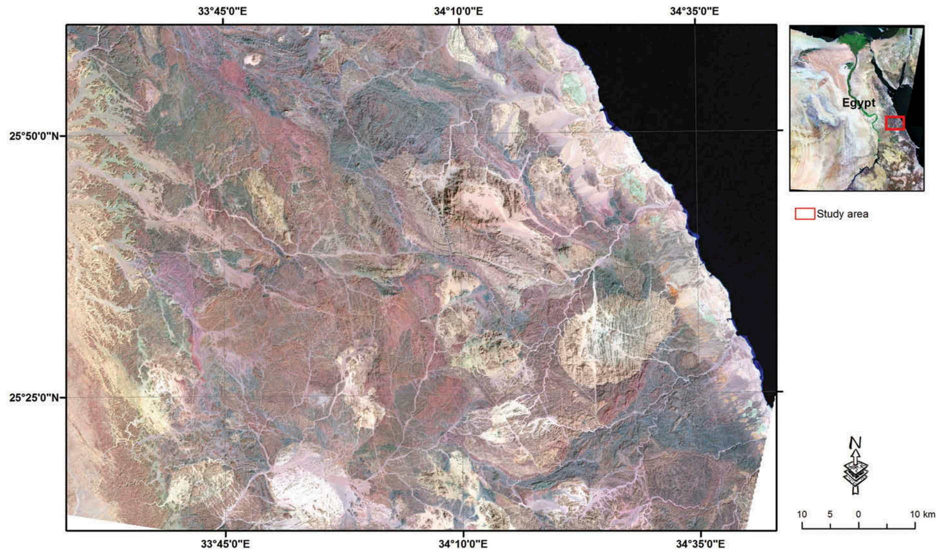

Figure 3. Landsat 7 ETM+ image of bands 742 in RGB showing the study area.

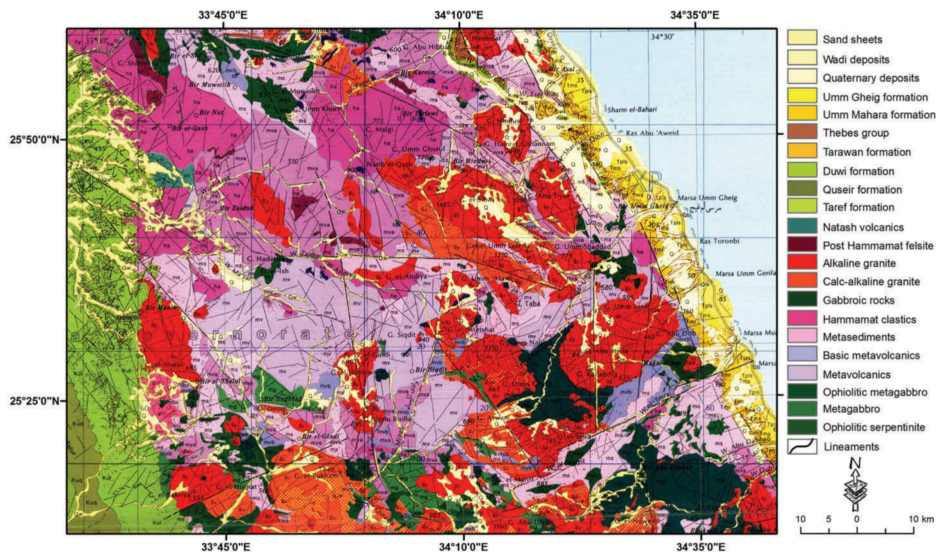

Figure 4. Geologic map of the study area modified from Conoco geological map 1987.

3. Material and methods

In this study, three data sets are implemented. The Enhanced Thematic Mapper Plus (ETM+) and the Advanced Spaceborne Thermal Emission and Reflection Radiometer (ASTER) multispectral data of path 174 and row 042 are available through the web portal: http://glovis.usgs.gov/. Table 1 summarizes the band information of the 30 m ETM+ and the 15 m ASTER data. In addition, we utilized spectral reflectance curves of the five main alteration minerals: haematite, illite, kaolinite, chlorite, and quartz

Table 1. Summary of ASTER and Landsat ETM+ sensor bands: the visible and near-infrared (VNIR), and shortwave infrared (SWIR).

	ASTER		ETM+	
Wavelength region	Band number (spatial resolution)	Spectral range (μm)	Band number (spatial resolution)	Spectral range (μm)
VNIR	1(15 m)	0.52–0.60	1(30 m)	0.45–0.52
	2(15 m)	0.63–0.69	2(30 m)	0.52–0.60
	3(15 m)	0.76–0.86	3(30 m)	0.63–0.69
SWIR	4(30 m)	1.60–1.70	4(30 m)	0.76–0.90
	5(30 m)	2.145–2.185	5(30 m)	1.55–1.75
	6(30 m)	2.185–2.225	7(30 m)	2.08–2.35
	7(30 m)	2.235–2.285		
	8(30 m)	2.295–2.365		
	9(30 m)	2.360–2.430		

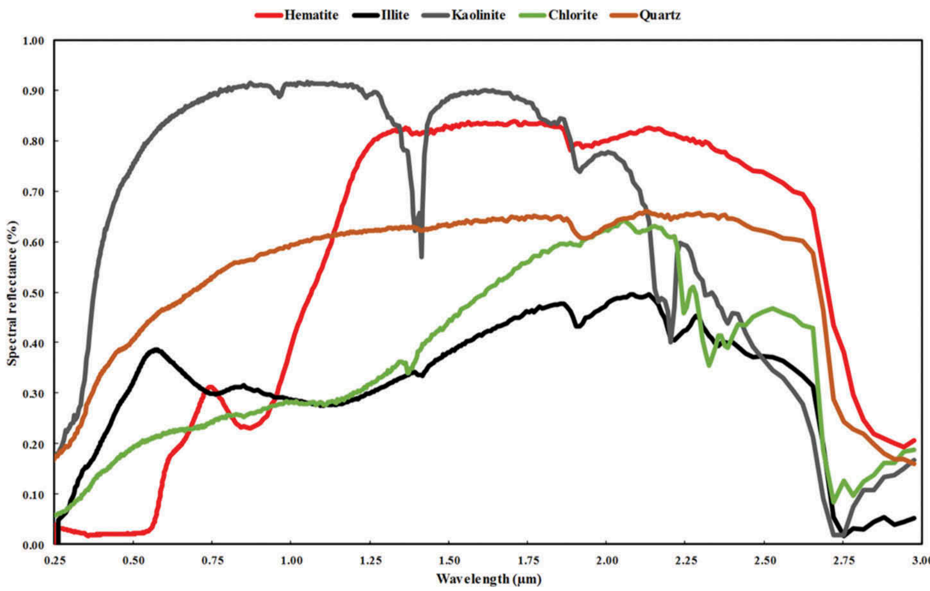

Figure 5. Spectral reflectance curves of the five main alteration minerals that were used as end-members for the SAM classification.

(Figure 5). The selected spectral minerals are the main indicators for the major wall-rock alterations that host gold deposits such as ferrugination, kaolinization, chloritization, and listwaenitization (Azer and Khalil 2005; Boyle 1979; El Ramly, Ivanov, and Kochin et al. 1970; Robert, Poulsen, and Dubé 1997). The spectral curves data are available from the United States Geological Survey (USGS) spectral library at http://speclab.cr.usgs.gov/spectral-lib.html. The USGS spectroscopy lab has measured the spectral reflectance of hundreds of materials, and the data has been available since 2007.

Finally, two total aeromagnetic maps recording the magnetic intensities of different rock units at the study area were utilized. To validate the results of the study, several global positioning system (GPS) points were collected around the actual mine locations. The chosen coordinate system of the GPS reading was Universal Transverse Mercator (UTM), zone 36 N with datum of World Geodetic System (WGS) 1984.

The data analyses include the following main steps: (1) atmospheric correction of Landsat ETM+ and ASTER images; (2) applying the SAM classification on the new composite bands using the five spectral reflectance curves; (3) interpolating the digitized and the geometrically corrected magnetic maps, and using the Euler deconvolution filter to detect the source depths of the faults; (4) delineating the lineation features using the ETM+ data to prepare the surface lineation map; (5) buffering, conversion, and reclassification of the all data sets into 0 and 1 binary images; and (6) using the fuzzy membership and fuzzy overlay operations, which are available from the SDM extension in ArcGIS 10.1 software to produce a predictive map for possible alteration areas. The workflow is summarized in Figure 6.

The ETM+ and the ASTER sensors' data were atmospherically corrected using the Fast Line-of-sight Atmospheric Analysis of Spectral Hypercubes (FLAASH) module in the Exelis Environment Visual Information (ENVI) 5.0 image processing software (Matthew, Adler–Golden, and Berk 2000). The digital numbers were converted into raw radiance and re-scaled to reflectance values that match the spectral reflectance curves of the alteration minerals. The nearest neighbourhood resampling technique was used to scale up the ASTER bands to the ETM+ cell size. This resampling method was chosen as it preserves the reflectance values of the newly aggregated ASTER bands. Layer stacking was applied, and the new bands were composites as listed in Table 2.

The SAM classification utilized the new composite bands, and the spectral curves of haematite, illite, kaolinite, chlorite, and quartz are used as end-members. The resulting

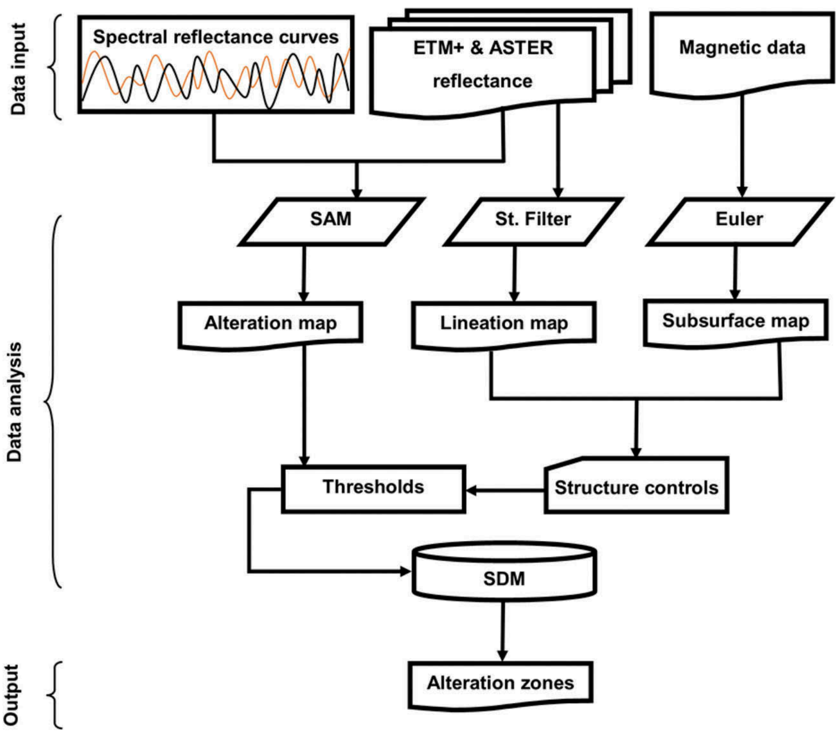

Figure 6. Methodology workflow. Abbreviations: St. Filter, structural filter; SDM, Spatial Data Modeler.

Table 2. New composite band list using ASTER and Landsat ETM+ sensors bands: the visible (Vis), near infrared (NIR), and shortwave infrared (SWIR).

	New composite bands	
Wavelength region	Band number (Sensor)	Spectral range (μm)
Vis	1(ETM+)	0.45–0.52
	1(ASTER)	0.52–0.60
	2(ETM+)	0.52–0.60
	3(ETM+)	0.63–069
NIR	3(ASTER)	0.76–0.86
	4(ETM+)	0.76–0.90
SWIR	4(ASTER)	1.60–1.70
	5(ETM+)	1.55–1.75
	7(ETM+)	2.08–2.35
	5(ASTER)	2.145–2.185
	6(ASTER)	2.185–2.225
	7(ASTER)	2.235–2.285
	8(ASTER)	2.295–2.365
	9(ASTER)	2.360–2.430

SAM layers initially contain two main classes: the unclassified class and the classified mineral values. To build the layers' attributes, the unclassified values were assigned to 0, and the classified alteration value was assigned to 1; then a new binary image of (0,1) was obtained. Ultimately, the five SAM images, each corresponding to an individual spectral curve, are intersected together using the Time operation in the ArcGIS map algebra toolbox to obtain a single alteration layer.

The information about the structural elements was delineated and determined using the ETM+, along with magnetic data. The resulting surface lineation, faults, and shear zones were confirmed through field excursions and the number of quadrangle geologic maps of scale 1:100,000 published by the Egyptian Geological Survey and Mining Authority (EGSMA 1989). In addition, the general geologic information was derived using the Conoco Coral geologic map sheet map of scale 1:500,000 (NG 36 SE Gabel Hammata). This map is available through the Egyptian General Petroleum Corporation (EGPC), and was published in 1987 (Conco 1987).

Meanwhile, the subsurface structure was detected using the magnetic data sets; two compiled sheets of total magnetic intensities maps were inputted into the GIS environment and digitized using the ArcScan module in ArcGIS 10.1 software. The data were georeferenced to the UTM projection of WGS 84, zone 36 N, and their attributes were built. Further processing was performed using Oasis montaj Geosoft 7.5 software. The data was interpolated using the natural neighbourhood technique. The Euler deconvolution filter was applied using a structure index of 1 to map the subsurface faults. The deep-seated faults were categorized according to their magnetic depths and overlaid to define the continuity of the subsurface structures.

To trace the migratory faulting systems, multiple ring buffers of radii 100 and 200 m were applied to the surface lineation, the shear zones, and the subsurface faults. These buffer ranges were selected because most of the fault systems are not vertical and therefore should have a dip angle. Thus, to ensure that all of the possible directions are included, the analysis process started with a wide radius. Then, using fuzzy logic classification, the buffered layers were categorized on a scale from 0 to 1 using an interval of 10 m. For larger radii, a lower rank was assigned, e.g. for a 200 m radius, the rank was 0. Then, the fuzzy overlay analysis tool was used to combine the SAM and structural layers, and thus ultimately determine the potential alteration sites. The fuzzy overlay combined evidence from each input using the two extremes of 0 (no probability) and 1 (highest probability) according to the following expression:

$$f = C_1 \bigcap C_2 \bigcap C_n, \tag{1}$$

where f is the fuzzy set of the intersection between criterion one (C_1) and criterion two (C_2) up to *n*-criteria.

The fuzzy set is calculated using the (min) operator of each membership grade of χ as follows:

$$f(\chi) = \min_j \left[C_j(\chi) \right]. \tag{2}$$

Meanwhile, the overall fuzzy decision function is based on the biggest f (χ). Therefore, the fuzzy gamma value was thresholded to 0.8. This allows the confining of the mapping to the geological contacts and a better determination of target alteration features at a higher confidence interval ranging from 85% to 95%.

4. Results and discussion

The SAM technique, along with the structural elements from ETM+ and aeromagnetic data, provides valuable results in terms of alteration zone mapping. The minerals' reflectance curves are the main indicators for the alteration zones. For instance, haematite and illite are the main iron oxide minerals in the ferrugination alteration zone. The kaolinite mineral is the main component of the kaolinization alteration zone. The chlorite mineral represents the chloritization that is often seen in the green-schist facies belt. Finally, silicon dioxide (quartz) characterizes the listwaenitization alteration zone. Figure 7 shows the five SAM alteration layers; both chlorite- and quartz-related alteration zones are the most dominant alteration types in the study area. The main reason is being related to the occurrence of the greenschist facies and granitic rocks. For instance, the serpentinite and ophiolite members are characterized by the abundance of green minerals such as chlorite, hornblende, pyroxene, biotite, and mica. The kaolinite and iron oxides are less-frequent alteration types and were seen as patches within the rocks.

Indeed, the structural elements from the surface lineation and subsurface faults are the main alteration controls. The delineated surface lineation and the shear zone displayed two major structural trends: the NW–SE trend that is generally related to the Najd fault system braids; and the NE–SW trend that represents the southern thrust serpentinite belt. Some of the shearing systems displayed a curvy pattern and waved around the boundary of the old granitic plutons (Figure 7).

The magnetic intensities of the structural elements and the rock covers are distinctly distinguished as shown in Figure 8. The total magnetic response over Nubian sandstone in the west, the dispersed granite plutons, metavolcanics, and serpentines appears to be completely identified. High magnetic intensities characterized the ultramafic and mafic rocks, whereas the acidic rocks are recognizable by their low magnetic responses. The magnetic anomalies over the study area revealed three major tectonic regimes: the southern serpentinites thrust, the middle graben with extensive granite intrusions, and

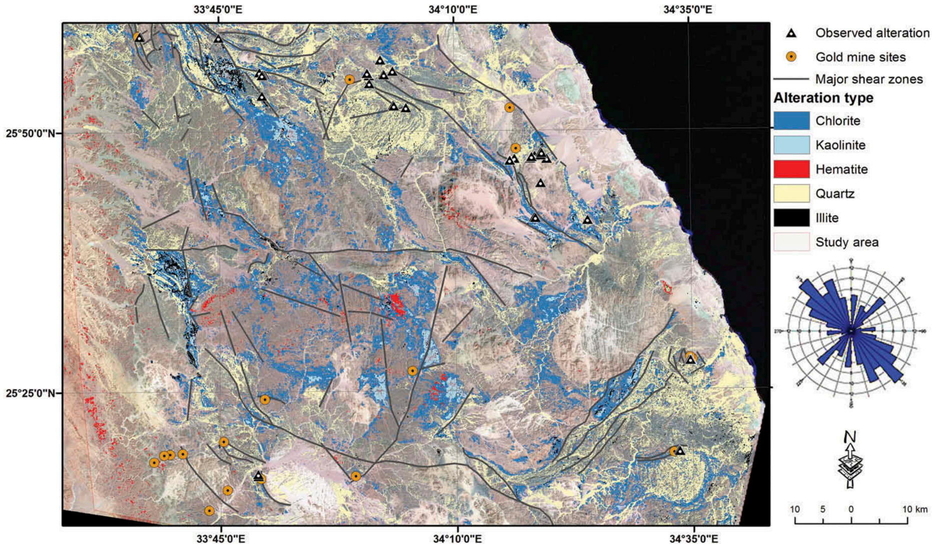

Figure 7. The SAM classification results along with the major surface shear zones. The rose diagram shows the major structural trends of the running shear zones.

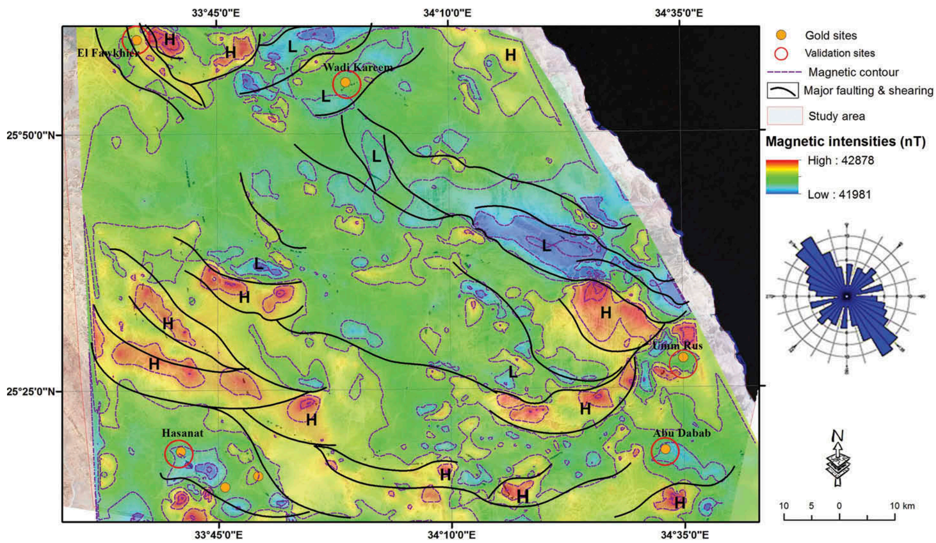

Figure 8. Structural and geologic interpretation of the total magnetic anomalies; the rose diagram shows the dominated shear trend in the area.

the northern thrust belt. The southern thrusting belt is characterized by the extensive existence of serpentinites and metavolcanic plutons, with elongated-shaped anomalies that strike from the east side of the study area towards the ENE–WSW direction and warp into the NW–SE direction as it goes towards the west part. All of these have almost high magnetic anomalies with amplitudes ranging between 42,600 and 42,800 Nanotesla (nT). All of the high magnetic anomalies are mainly related to ophiolites mélange and the basic metavolcanic rocks. The central part of the study area is characterized by low magnetic intensities within the range 41,200–42,400 nT; the amplitude of these anomalies is related to the magnetic response of molass sediments, granites, and acidic metavolcanic rocks. The northern part of the study area is dominated by another appearance of high magnetic amplitudes that are related to the ambaji metavolcanics in the northeast side (marked by the letter H) and the serpentinites around the Fawkhier area in the far west.

Faulting and geologic causal relationships were detected by applying the 3D Euler deconvolution solution on the total aeromagnetic intensities. The Euler deconvolution filter is applied to locate the depths of different structural windows according to a specific structural index (Hsu 2002; Rabeh et al. 2006; Reid et al. 1990). The selected structural index of 1 was selected to detect the depths of the anomalies related to the deep-seated faults and the linear contacts. The estimated depths to the linear structures inferred that the depths ranged between 500 m and 2000 m (Figure 9), and as the depths increased, the linearity pattern becomes distinctly remarkable.

The complementary interpretation of surface lineation and the subsurface faults helps identify the favourable pathways for hydrothermal solution that formed the different alteration types. SAM classification and the structural controls were mainly overlaid, and together constituted the main inputs for the fuzzy membership classification to identify a single data set, indicating the possible alteration locations. The result showed that the alteration zones are mainly striking, follow the dominated structural elements, and are aligned within the serpentinite contact, as is shown in Figure 10. To validate our results, several GPS points were collected around the actual mineralized sites: Fawkhier gold mine, Wadi Kareem, Umm Rus mine Abu Dabab occurrence, and Hasant gold mine (Figure 10). The comparison of the proposed mapping results showed high agreement between the known alteration sites and the current mapped locations. The analysis of the remote-sensing data and magnetic maps helped identify new promising sites for

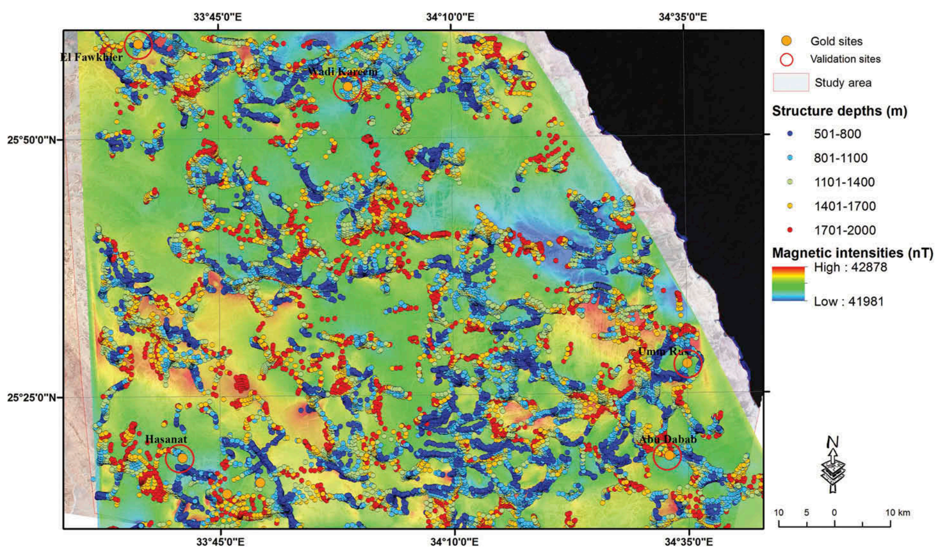

Figure 9. 3D Euler deconvolution filter of the deep faults ranging from 500 m to 2000 m.

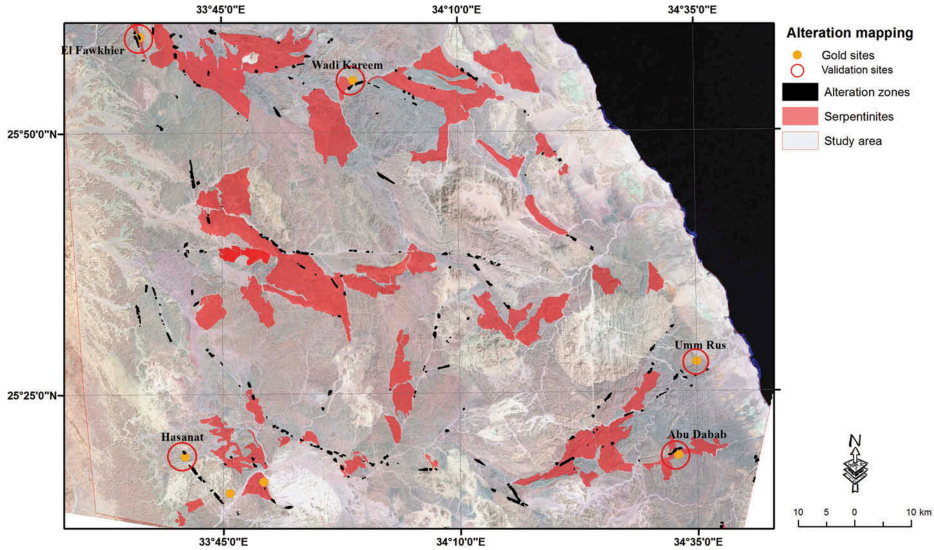

Figure 10. New promising gold mineralization sites. The red circles are around the actual validation sites that have mineralized alterations.

gold minerals in CED. The current research results open great opportunities for further exploration and mining activities in CED, Egypt.

5. Conclusion

Alteration zones are considered the most promising areas for mineral exploration in CED. Ancient gold miners in Egypt were only targeting the smoky quartz veins that contain large amounts of gold; however, they left the alteration areas untouched. Remote sensing and geophysical techniques can provide cost-effective tools that can give valuable information about the new mineralization sites. SAM classification is one of the powerful classification techniques that can be integrated with aeromagnetic data to map the potential gold sites associated within the alteration zone in CED. In the current work, five main spectral alteration minerals' curves are used as an end-member for the SAM classification. To aid in better mapping, the SAM result is constrained by the structural elements that restrict the mapping to the actual alteration sites. The surface lineation and the total magnetic intensities were deployed to understand the tectonic regimes in the study area, and the structural patterns. The analysis of the total magnetic intensities revealed three major dominant magnetic regimes in the study area: the sheared serpentinite and basic rocks, which is characterized by high magnetic anomalies, and strikes towards ENE–WSW from the east corner, which deviated towards the NW–SE directions; the middle magnetic anomalies with low intensities related to the clustering of granites and acidic metavolcanics; and the northern magnetic anomalies with high intensities related to the serpentines around Fawkhier gold mine in the west and patches of basic metavolcanics on the east side. Since the alterations are formed along a structural element, applying a 3D Euler deconvolution filter can provide the required tool to map the deep-seated faults. The Euler deconvolution filter located the deep-seated faults by assigning a structural index of 1. The intersection between the surface and subsurface structures introduced the possible migration paths for hydrothermal solutions. The fuzzy membership classification and the fuzzy overlay tools are available through the advanced SDM geoprocessing extension. Both were used to produce a predicative map according to the categorical inputs. The results showed the possible locations that can be considered as future targets for mineral exploration in CED. The results are confirmed using the actual GPS reading from existing mineralization sites. We believe that the SAM classifier can potentially be a powerful tool, and provides valuable information for alteration zone mapping with aeromagnetic data.

Acknowledgements

The first author acknowledges the Mission sector of the Egyptian Ministry of Higher Education and Scientific research for providing the financial support to conduct this research in the USA through a PhD scholarship. Thanks goes to the Advanced Radar Research Center (ARRC) group and the Hydrometrology and Remote Sensing Laboratory (HyDROS) research group at the University of Oklahoma (OU) for providing the research facilities and lab equipment for this work. We really appreciate the comments of two anonymous reviewers that helped us improve the overall quality of the manuscript. Additionally, thanks goes to the OU writing center and to Race Clark for their help in the manuscript proofreading and the English corrections.

The ETM+ and ASTER data sets are obtained from the Land Processes Distributed Active Archive Center (LP DAAC), and the spectral reflectance curves are obtained from the USGS.

Disclosure statement

No potential conflict of interest was reported by the authors.

Funding

The author would like to thank the Mission sector of the Egyptian Ministry of Higher Education and Scientific research for providing the financial support to conduct this research in the USA through a PhD scholarship.

ORCID

Emad Hasan http://orcid.org/0000-0002-8337-0423

Reference

Amer, R., T. Kusky, and A. El Mezayen. 2012. "Remote Sensing Detection of Gold Related Alteration Zones in Um Rus Area, Central Eastern Desert of Egypt." *Advances in Space Research* 49 (1): 121–134. doi:10.1016/j.asr.2011.09.024.

Azer, M. K., and A. E. S. Khalil. 2005. "Petrological and Mineralogical Studies of Pan-African Serpentinites at Bir Al-Edeid Area, Central Eastern Desert, Egypt." *Journal of African Earth Sciences* 43 (5): 525–536. doi:10.1016/j.jafrearsci.2005.09.008.

Botros, N. S. 2004. "A New Classification of the Gold Deposits of Egypt." *Ore Geology Reviews* 25: 1–37. doi:10.1016/j.oregeorev.2003.07.002.

Boyle, R. W. 1979. "The Geochemistry of Gold and Its Deposits." *Geological Survey of Canda, Bulliten* 280: 584.
Conco. 1987. *Geologic map of Egypt (NG 36 SE Gabal Hammata) scale 1:500.000*. Cairo, Egypt: Egyptian General Petroleum Corporation (EGPC).
EGSMA. 1989. *Geologic Maps Quadrangle NG 36 SE Scale 1:100.000*. E. G. Survey, Editor. Cairo, Egypt: Salah Salem Road Abbassiya.
El Ramly, M. F., S. S. Ivanov, and G. G. Kochin. 1970. "The Occurrence of Gold in Eastern Desert of Egypt." In *Studies on Some Mineral Deposits of Egypt*, edited by O. Moharram, 53–64. Cairo: Geological Survey of Egypt.
EMRA. 2006. *Gold in Egypt, Potentiality of Bid round Blocks (Part II)*. Cairo: Egyptian Mineral Resources Authority.
ENVI. 2008. *User's Guide. ENVI On-line Software User's Manual, ITT Visual Information Solutions*. Boulder, CO: Exelis Visual Information Solution.
Gabr, S., A. Ghulam, and T. Kusky. 2010. "Detecting Areas of High-Potential Gold Mineralization Using ASTER Data." *Ore Geology Reviews* 38 (1–2): 59–69. doi:10.1016/j.oregeorev.2010.05.007.
Gad, S., and T. Kusky. 2006. "Lithological Mapping in the Eastern Desert of Egypt, the Barramiya Area, Using Landsat Thematic Mapper (TM)." *Journal of African Earth Sciences* 44 (2): 196–202. doi:10.1016/j.jafrearsci.2005.10.014.
Gad, S., and T. Kusky. 2007. "ASTER Spectral Ratioing for Lithological Mapping in the Arabian–Nubian Shield, the Neoproterozoic Wadi Kid Area, Sinai, Egypt." *Gondwana Research* 11 (3): 326–335. doi:10.1016/j.gr.2006.02.010.
Gupta, R. P. 2003. *Remote Sensing Geology*. Berlin, Heidelberg, New York: Springer-Verlag.
Honarmand, M., H. Ranjbar, and J. Shahabpour. 2012. "Application of Principal Component Analysis and Spectral Angle Mapper in the Mapping of Hydrothermal Alteration in the Jebal-Barez Area, Southeastern Iran." *Resource Geology* 62 (2): 119–139. doi:10.1111/rge.2012.62.issue-2.
Hoover, D. B., D. P. Klein, and D. C. Campbell. 1995. *Geophysical Methods in Exploration and Mineral Environmental Investigations. Preliminary Compilation of Descriptive Geoenvironmental Mineral Deposit Models*. Denver, CO: U.S. Geological Survey.
Hsu, S. K. 2002. "Imaging Magnetic Sources Using Euler's Equation." *Geophysical Prospective* 50 (1): 15–25. doi:10.1046/j.1365-2478.2001.00282.x.
Hunter, E. L., and C. H. Power. 2002. "An Assessment of Two Classification Methods for Mapping Thames Estuary Intertidal Habitats Using CASI Data." *International Journal of Remote Sensing* 23: 2989–3008. doi:10.1080/01431160110075596.
Hussien, A. A. 1990. "Mineral Deposits of Egypt." In *The Geology of Egypt*, edited by R. Said, 511–566. Rotterdam: A. A. Balkema Publishers.
Kainz, W. 2007. *Fuzzy Logic and GIS*. Vienna: University of Vienna.
Klemm, D., R. Klemm, and A. Murr. 2001. "Gold of the Pharaohs – 6000 Years of Gold Mining in Egypt and Nubia." *Journal of African Earth Sciences* 33: 643–659. doi:10.1016/S0899-5362(01)00094-X.
Kruse, F. A., J. W. Boardman, A. B. Lefkoff, K. B. Heidebrecht, A. T. Shapiro, P. J. Barloon, and A. F. H. Goetz. 1993. "The Spectral Image Processing System (SIPS) Interactive Visualization and Analysis of Imaging Spectrometer Data." *Remote Sensing of Environment* 44: 145–163. doi:10.1016/0034-4257(93)90013-N.
Kruse, F. A., L. L. Richardson, and V. G. Ambrosia. 1997. "Techniques Developed for Geologic Analysis of Hyperspectral Data Applied to Near-Shore Hyperspectral Ocean Data." Presented at the Fourth International Conference on Remote Sensing for Marine and Coastal Environments, Orlando, FL, March 17–19.
Matthew, M. W., S. M. Adler–Golden, and A. Berk. 2000. "Status of Atmospheric Correction Using a MODTRAN4–Based Algorithm." *In Proceedings of Algorithms for Multispectral, Hyperspectral, and Ultraspectral Imagery, SPIE* 4049: 199–207.
McMahon, J. M. 1979. "Primary and Secondary Faulting in the Najd Fault System, Kingdom of Saudi Arabia." U.S. Geological Survey Saudi Arabian Project Report 262. U.S. Geological Survey. Accessed 16 November 2010. http://pubs.usgs.gov/of/1979/1661/report.pdf.

Papp, E., and T. Cudahy. 2002. “Hyperspectral Remote Sensing, Geophysical and Remote Sensing Methods for Regolith Exploration (E. Papp, Editor).” CRCLEME Open File Report, 13–21.

Pour, A. B., and M. Hashim. 2012. “The Application of ASTER Remote Sensing Data to Porphyry Copper and Epithermal Gold Deposits.” *Ore Geology Reviews* 44: 1–9. doi:10.1016/j.oregeorev.2011.09.009.

Rabeh, T., K. O. El Faragawy, A. M. Menasiy, and J. M. Miranda. 2006. “The Role of Geomagnetic Method in Detecting the Structural Control of Mineral Deposits at El-Hudy Area.” Southeastern Aswan, Egypt. Proceedings of 4th International Symposium on Geophysics, Tanta University, Tanta, January 20, 251–266.

Ramadan, T. M., and S. A. Sultan. 2003. “Integration of Geological, Remote Sensing and Geophysical Data for the Identification of Massive Sulphide Zones at Wadi Allaqi Area.” South Eastern Desert. Egypt: IEEE, 0-7803-7929, 2589–2591.

Reid, A. B., J. M. Allsop, H. Ganser, A. J. Millet, and I. W. Somerton. 1990. “Magnetic Interpretation in Three Dimensions Using Euler Deconvolution.” *Geophysics* 55: 80–91. doi:10.1190/1.1442774.

Ren, D., and M. G. Abdelsalam. 2006. “Tracing Along-Strike Structural Continuity in the Neoproterozoic Allaqi-Heiani Suture, Southern Egypt Using Principal Component Analysis (PCA), Fast Fourier Transform (FFT), and Redundant Wavelet Transform (RWT) of ASTER Data.” *Journal of African Earth Sciences* 44 (2): 181–195. doi:10.1016/j.jafrearsci.2005.10.010.

Robert, F., K. H. Poulsen, and B. Dubé. 1997. “Gold Deposits and Their Geological Classification.” In *Proceedings of Exploration 97: Fourth Decennial International Conference on Mineral Exploration* edited by A. G. Gubins, 209–220. Toronto, ON: Prospectors and Developers Association of Canada.

Sawatzky, D., G. Raines, and G. Bonham-Carter. 2010. “Spatial Data Modeller.” Accessed 6 July 2010. http://www.ige.unicamp.br/sdm/ArcSDM10/source/ReadMe.pdf

Telford, W. M., L. P. Geldart, and R. E. Sheriff. 2001. *3. Magnetic Methods. Applied geophysics*. Cambridge: Cambridge Univ. Press.

Yager, R. R. 2015. “Fuzzy Methods for Constructing Multi-Criteria Decision Functions.” International Institute for Applied Systems Analysis (IIASA) System Anlaysis 2015 Conference, Laxenburg, November 11–13.